

## Research Article

# Numerical Analysis of Subgrade Behavior under a Dynamic Maglev Train Load

Wubin Wang <sup>1,2</sup>, Zhixing Deng <sup>2</sup>, Yandong Li <sup>2</sup>, Zhichao Huang <sup>2</sup>, Yunbin Niu <sup>2</sup>,  
and Kang Xie <sup>3</sup>

<sup>1</sup>National Engineering Laboratory for Technology of Geological Disaster Prevention, Land Transportation, Southwest Jiaotong University, Chengdu 611731, China

<sup>2</sup>School of Civil Engineering, Southwest Jiaotong University, Chengdu, Sichuan 610031, China

<sup>3</sup>Department of Civil Engineering, Central South University, Changsha 410075, China

Correspondence should be addressed to Kang Xie; [xiekang1995@outlook.com](mailto:xiekang1995@outlook.com)

Received 7 July 2021; Revised 7 December 2021; Accepted 22 February 2022; Published 11 May 2022

Academic Editor: Wenjie Ge

Copyright © 2022 Wubin Wang et al. This is an open access article distributed under the Creative Commons Attribution License, which permits unrestricted use, distribution, and reproduction in any medium, provided the original work is properly cited.

Medium-low-speed maglevs are increasingly used in the urban rail transit industry because of their advantages, such as low noise and low energy consumption. In this study, a finite element analysis of the responses of the subgrade that supports a medium-low-speed maglev structure under a dynamic maglev load is presented. First, the finite element analysis considers a low-lying structure with different elastic moduli. Then, the attenuation laws of the dynamic stress and dynamic deformation for different depth ranges of the subgrade under the rail beam are analyzed. In addition, the magnitude of the influence of the dynamic load is clarified. The results lead to a recommendation of a base bed thickness of 1.5 m, graded gravel or group A filler as the surface layer of filler, and gravel soil as the bottom layer. This study provides theoretical support for the construction design of a subgrade structure under the rail beam of a low-lying maglev line.

## 1. Introduction

A maglev transportation system is a rail transit system that uses electromagnetic force to keep trains and tracks out of contact [1]. As a new type of rail transportation system, maglev transportation has good prospects for application in urban transportation, regional traffic, intercity traffic, and the national backbone network [2]. Medium-low-speed (MLS) maglev traffic refers to a traffic system whose maximum operating speed does not exceed 160 km/h [3].

Since MLS maglev rail transit has advantages of low noise, low vibration, low energy consumption, and strong adaptability to tight curves and steep slopes [4–6], this configuration is increasingly used in the urban rail transit industry [7, 8]. It is important to design a proper superstructure and substructures in rail transport systems. Relevant research has examined the use of ballast-less track systems [9] and metro track systems [10] to improve the reliability of design and reduce the impact of vibration on

the environment. However, MLS maglev rail transit systems mostly use the overhead line method, and there are few application examples of low-lying structures where rail beams are placed directly on the subgrade [11]. Past MLS maglev line engineering research has mainly focused on overpasses [12], and further research on low-lying structures between the overhead line and the underground line is needed. Additionally, there is still a lack of relevant research and technical standards for the beds of MLS maglev subgrade structures.

At present, related scholars have conducted many studies on the dynamic response of the low-set roadbed structure of low and medium-speed magnetic levitation: relying on the Zhuzhou test line, China Railway Second Institute Engineering Group Co., Ltd., analyzed and tested the stress of the roadbed under the bearing rail beam through simulation analysis and field running tests, and derived the stress distribution law of the roadbed filler under the train load [13]. Cai and Yang analyzed and studied the

key technologies of track design, track beam stiffness, and dynamic coefficient of the test line by simulation analysis combined with Zhuzhou field running test, respectively [14, 15]; Gao analyzed and tested the stress of track beam and roadbed under the track beam by field test [16]; Li's team from Southwest Jiaotong University cooperated with China Railway Fourth Survey and Design Institute Group Co. Ltd., has carried out an in-depth study on the coupled dynamics of magnetic levitation vehicles and rails, and has conducted a systematic study on the dynamic characteristics of the low-set structure roadbed. The vibration response under the vehicle-low-mounted beam coupling was obtained by the field running test combined with numerical simulation by Li and Wang, respectively [17, 18]. At present, the technical standards for subgrade beds for MLS maglev structures, such as the use of padding and their compaction standards [19], are formulated mainly with reference to the technical standards for subgrade beds for high-speed railways [20]. Therefore, the above-mentioned series of studies were also conducted on this basis. Research on subgrade beds of MLS maglev low-lying structures based on speeds of 120 km/h and 160 km/h is still lacking. However, MLS maglev systems are quite different from high-speed railway systems in their load action mode, load intensity, and transmission method of the system structural force [21]. Fully referring to the high-speed railway design code [22] would cause certain deviations and greater safety reserves. Thus, it is necessary to further study the dynamic behaviors of subgrade beds under different speed standards according to the characteristics of MLS maglev rail transit projects [23].

The main focus of this paper is the MLS maglev subgrade for low-lying structures. The commercial finite element analysis software ABAQUS [24] is used to conduct finite element analysis of low-lying structures with different elastic moduli and to analyze the attenuation of the dynamic stress and deformation of the subgrade. In addition, the analyses of the trends of dynamic stress and dynamic deformation in different depth ranges of the subgrade under the rail beam are also implemented by ABAQUS. Finally, the magnitude of the influence of the dynamic load and theoretical support for the construction design of a subgrade structure under the rail beam of a low-lying maglev line are clarified.

## 2. Review of Existing MLS Maglev Systems

Typical MLS maglev lines include the Aichi High-Speed Transit Tobu Kyuryo Line in Japan [25], the Incheon Airport Maglev in South Korea [26], and the MLS Test Line (rail holding car) of The German Company Borg [27], as shown in Figure 1.

Since the beginning of the twenty-first century, there have been some relevant studies on MLS maglev technology, and several test lines have been successively built, including the Changsha Test Line of the National University of Defense Technology [29], the Qingchengshan Test Line of Southwest Jiaotong University [30], the Shanghai Lingang Test Line of Tongji University [31], the Tangshan test line [32], and the CRRC Zhuzhou test line [13]. On April 5, 2002, a MLS maglev test line developed and built by the National University of Defense Technology and other institutions was

opened to traffic in Changsha [23]. The test line is 204 m in length, including a 100 m radius curve and a gradient of 4%, with a gauge width of 2 m. The coach is 15 m long and can carry more than 130 passengers. It is designed to travel at a speed of 150 km/h. In 2003, Southwest Jiaotong University established the MLS maglev test line in Qingchengshan, Chengdu, Sichuan [30]. The maglev test track is 420 m long, and the coach is 11.2 m in length, 2.6 m in width, 3.3 m in height, and 18 t in weight. By the end of 2006, the Shanghai MLS maglev test line was completed, with a total length of approximately 1.5 km, and vehicle assembly and commissioning were also completed [31]. In November 2008, the Shanghai low-speed maglev line realized 85 km/h trial operation of three connected trains, and in December 2008, the line reached a 101 km/h trial operation speed. In June 2010, the Tangshan MLS maglev test line with a total length of 1547 m was completed [32]. This short test line of only approximately 1,000 m incorporates various features, such as a 70‰ gradient and 100 or 50 m radius space rotation and turning. In addition, the coach is 15 m in length and 3 m in width. The above test lines are shown in Figure 2.

However, these existing test lines did not adopt a low-lying structure in which the rail bearing beam is directly placed on the subgrade. In July 2012, the MLS maglev test line of Zhuzhou Locomotive Corporation, with a total length of 1.7 km, was completed and commissioned. Approximately 800 m of the line was adopted in the form of a rail bearing beam placed directly on the subgrade of a low-lying structure. Since the MLS maglev train suspension clearance, that is, the distance between the train and the track, is approximately 8 mm, the requirements of deformation of the offline structure, i.e., the line foundation system below the track, are more stringent than the traditional railway lines. At that time, worldwide consensus was that maglev rail transit should not adopt a low-lying structure of the subgrade; thus, at the beginning of the design of Zhuzhou test lines, there was a lack of research about the rail bearing beam of low-lying structures. Therefore, a conservative design was adopted: The subgrade was filled with graded gravel, the maximum filling height was approximately 4.0 m, and the subgrade base was reinforced with a composite foundation.

The Zhuzhou test line has been used to conduct research on low-lying structures [13], primarily on the rail bearing beam. The stress of the subgrade under the rail bearing beam has been analyzed and tested through simulation analysis and field driving tests only. The subgrade bed under the rail bearing beam has not been studied systematically. Based on the relevant research results of the Zhuzhou test line, the Changsha Maglev Express Line has optimized the design of the subgrade bed with a low-lying structure. The surface of the subgrade is made of 0.3 m thick graded gravel, and group A filler (the grouping standard of filler refers to the code for railway Earth subgrade design [34]) is used below the surface of the subgrade. The compaction standard adopted the compaction standard of a high-speed railway subgrade bed for reference. The main line section and depot section of the Changsha maglev line feature 6 sections of low-lying structures with a total length of approximately 1.2 km. Solid

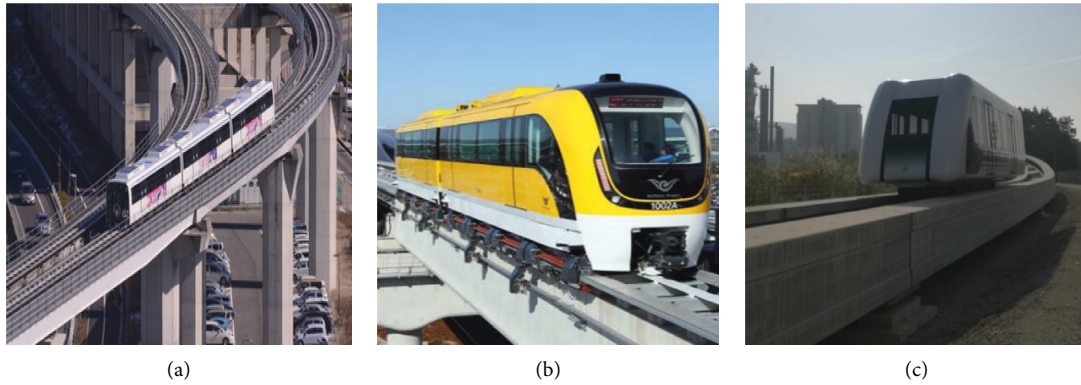


FIGURE 1: Typical MLS maglev lines: (a) Aichi High-Speed Line; (b) Incheon Airport Maglev; (c) MLS Test Line [12, 28].

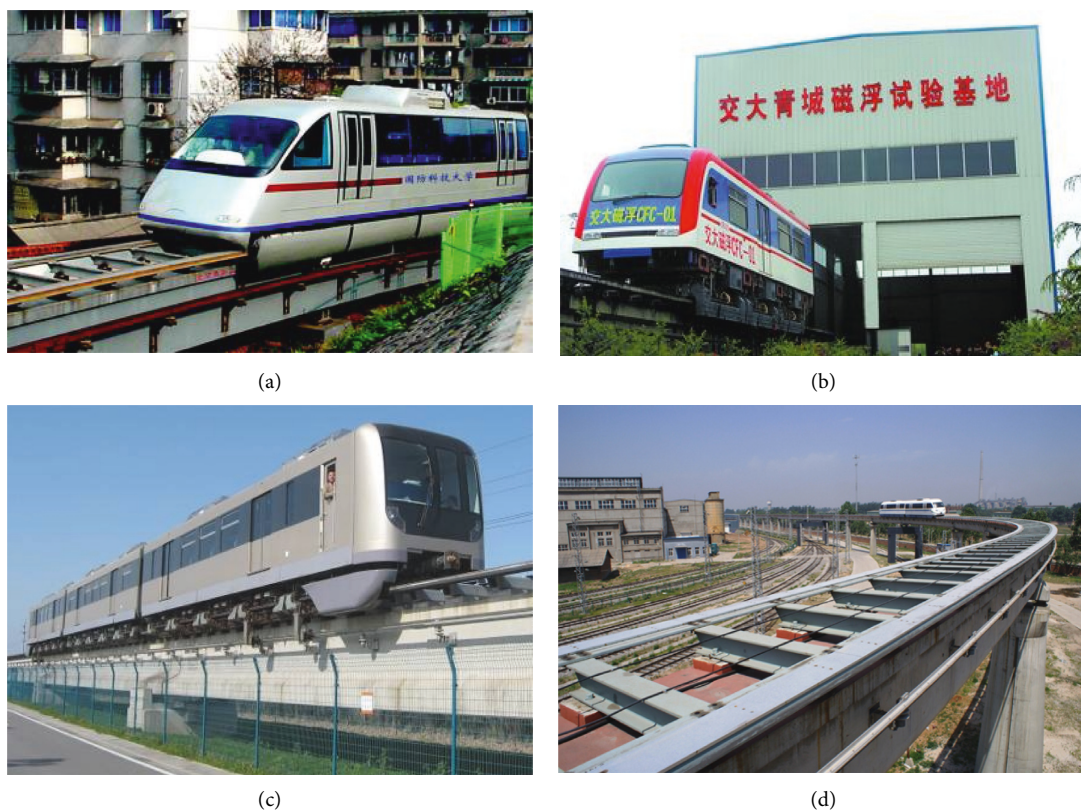


FIGURE 2: Mls maglev test lines: (a) Changsha test line; (b) Qingchengshan test line; (c) Shanghai Lingang test line; (d) Tangshan test line [3, 12, 33].

beams are used in the main line section, and frame column beams are used in the depot section. Two of these 6 sections are filled embankments with a height of approximately 3.5 m. This is the world's first MLS maglev operating line with a low-lying structure in which the rail beam is directly placed on the subgrade, thus breaking the technical restriction—originally maintained by experts worldwide—that maglev rail transit should not use low-lying structure subgrades. This design extends the geological and terrain conditions in which MLS maglev transportation can be applied, reduces engineering costs, and demonstrates leading-edge technology.

Relying on the Changsha Maglev Express Line, a systematic study was conducted on the subgrade bed of a low-lying structure [19]. The dynamic stress and deformation of the subgrade surface, the stiffness of the subgrade, the limit of the deformation of the subgrade, the dynamic strength of the subgrade, the design of the subgrade, and the thickness of the subgrade replacement of the cutting were studied. The related research on the Zhuzhou test line and Changsha Maglev Express Line involves the following main problems:

- (1) The research objects are all MLS maglev lines with a design speed of 100 km/h. Research on the subgrade

beds of MLS maglev lines with speeds of 120 km and 160 km is still lacking.

- (2) In the theoretical analysis, the dynamic coefficient adopts the calculation formula of the wheel-rail system, and the dynamic stress of the subgrade surface is considered at 30 kPa, while the measured maximum value on the Changsha Maglev Express Line and the Zhuzhou test line is approximately 10 kPa, which is too conservative [35].
- (3) The research adopted the compaction standards of high-speed railway filling but failed to conduct a systematic study on subgrade filling and compaction standards.
- (4) The influence of the backfill layer and cushion layer on the dynamic stress distribution along the depth of the subgrade was not considered.
- (5) The research results are still unable to provide comprehensive support for the technical standards of subgrade beds with low-lying structures. At present, the corresponding design, including filling and compaction standards and calculation of dynamic coefficients, mainly adopts the relevant technical standards of high-speed rail, which provide more safety reserves.

### 3. Numerical Modeling of a Maglev Train Subgrade Bed

To study the force and deformation of a subgrade bed under a maglev train load, a 3D numerical model is established based on finite element theory using ABAQUS. The upper part is a block-type rail bearing beam structure and track structure, which are further described in Section 3.2. The subgrade has a two-layer structure: the surface layer of the subgrade bed with a thickness of 0.3 m and the bottom layer of the subgrade with a thickness of 1.2 m. Numerical calculations are used to study whether the structure of the subgrade can meet the required deformation and strain control in this case. An overall three-dimensional model diagram is shown in Figure 3. The specific introduction is as follows.

*3.1. Development of the Model.* The model is established with the aim of simulating the actual situation as much as possible, with some simplification. In the model, the maglev train load is simplified as a uniformly distributed load, and the bolt connection of the fixed track is simplified as a binding contact. The track structure and the soil layer within the vibration range have linear elastic properties [36]. Therefore, in the finite element model (FEM), the track structure, the rail beam, and the surface filling of the subgrade bed are set as linear elastic models, and the other soil layers are set as Mohr-Coulomb elastic-plastic models. The size of the model is sufficiently large [37], and the length of the longitudinal dimension is 3 times the length of a single-section rail beam. The bottom surface of the model is a fixed boundary, and the side of the model restricts horizontal displacement. The data of the two side rail beams are

compared with the middle rail beam. In this study, the data of the middle rail beam was extracted and analyzed to reduce the influence of the boundary effect of the model. The grid of the model adopts a C3D8R eight-node linear hexahedral three-dimensional stress element, which reduces integrals and controls hourglass effects. The overall grid division is relatively regular with a total of 123783 nodes and 78172 elements. The base of the rail beam is in hard contact with the surface normal of the bed, the tangent is in contact with a penalty function, and binding constraints are used between other model components. When exploring the influence of dynamic load on the foundation bed, the gravity of the foundation bed and the foundation is not considered, but when analyzing the self-weight stress distribution of the depth of the dynamic load influence, gravity is considered. The dynamic implicit integral algorithm is adopted to simulate the running process from the head of the train entering the middle rail beam model to the end of the train leaving the model.

*3.2. Dimensions of the Model.* The upper rail beam structure of the model mainly comprises three parts: the top plate, the column and the base. In this model, three rail beams are established. The length of the base of each rail beam is 11.58 m, with a 20 mm expansion joint between each section. The bases are connected by dowel steel (Q235 steel,  $\phi 50 \times 5 \times 700$  mm), and the total length of the rail bearing beam base is 34.78 m. The spacing between the blocks is 1.2 m, and the specific structural dimensions are shown in Figure 4.

The upper part of the supporting rail beam is equipped with a track structure. Above the top plate is an H-shaped rail, which is connected by backing plates and gaskets as shown in Figure 5. In this simulation, the different parts are connected by binding instead of bolts. The F-shaped rail is laid longitudinally at the two ends of the H-shaped rail and is loaded to simulate the load of the actual maglev train.

The subgrade structure is composed mainly of a subgrade surface layer, a subgrade bottom layer, and its underlying filled layers. The total thickness of the embankment is 3 m, the thickness of the lower base model is 2.5 m, and the subgrade structure is modeled with a slope of 1:1.5. Considering the influence of the boundary conditions, a sufficient width of the base soil is set to reduce the influence of the boundary on the centerline of the line. There is a 0.1 m thick concrete cushion on the surface of the base bed and a rail bearing beam structure above the cushion. A backfill soil layer is set around the base of the rail bearing beam. The overall length of the model is 36.8 m, and the width is 20.5 m. The schematic diagram is provided in Figure 6.

*3.3. Material Properties.* The structural properties of the subgrade bed are determined according to the theoretical analysis. The Mohr-Coulomb model is selected to define the elastoplastic behavior of soils. Therefore, the deformation modulus is used as its modulus parameter. The properties are shown in Table 1.

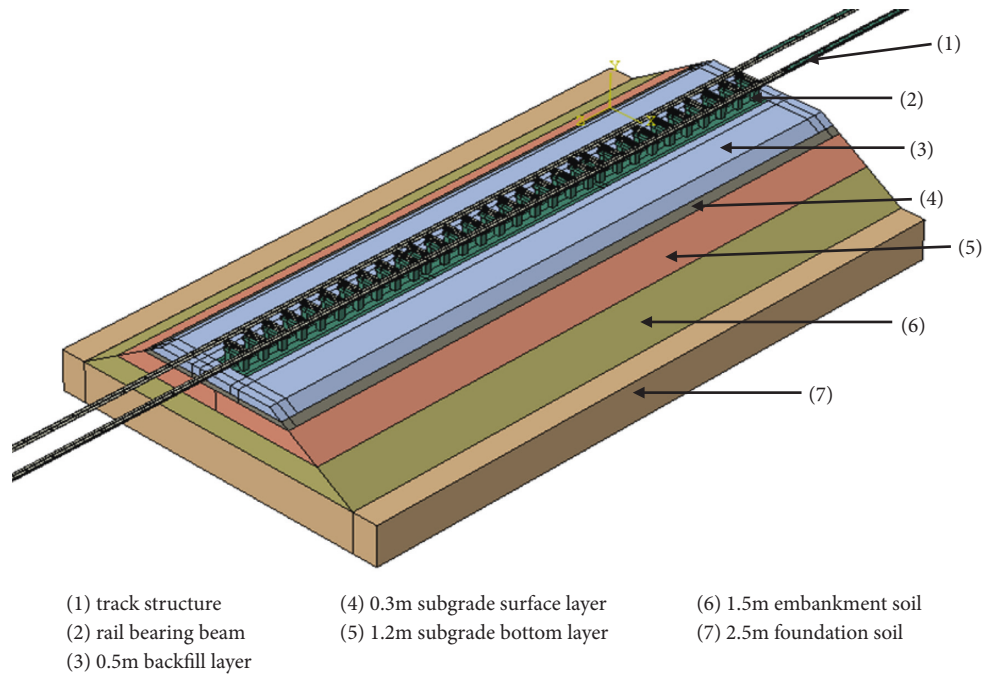


FIGURE 3: Three-dimensional model diagram.

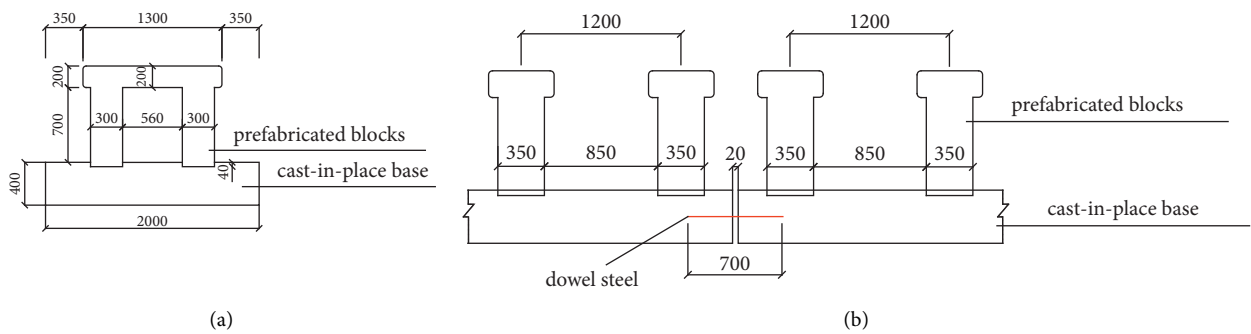


FIGURE 4: Rail beam specific structural dimensions (unit: mm); (a) cross-sectional diagram; (b) longitudinal diagram.

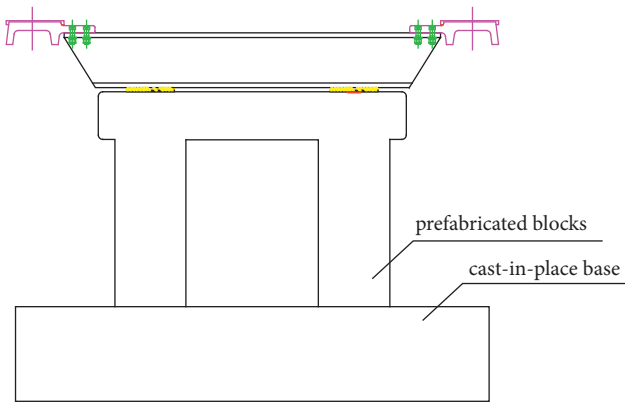


FIGURE 5: Cross-sectional diagram of the track and rail bearing beam.

**3.4. Loading.** The load acting on the top surface of the rail beam mainly includes the dead load and the vertical live load of the train. The dead load includes the self-weight of the rail

beam structure and the self-weight of the track structure acting on the rail beam. According to the design achievements of Changsha Maglev Express and Qingyuan Maglev, the height of the track structure is 0.292 m (excluding the track platform), and the dead weight of the track structure is shown in Table 2.

The calculation shows that the dead load value is approximately 4.5 kN/m. In this simulation, this dead load is applied by the gravity method of the track structure. According to the “Basic Technical Parameters of Changsha Maglev Vehicles” [38], the load of a single train in suspension is as shown in Figure 5, and the uniform load is 12.9 kN/m. Therefore, the actual simulated load in the model is as shown in Figure 7. There are three trains in total, and the distance between each train is 1.68 m. According to the actual load width of the F-shaped rail subjected to the maglev train, a load with a width of 0.218 m is established in the model, which is converted into an area load of 59.174 kPa, which is taken as 60 kPa.

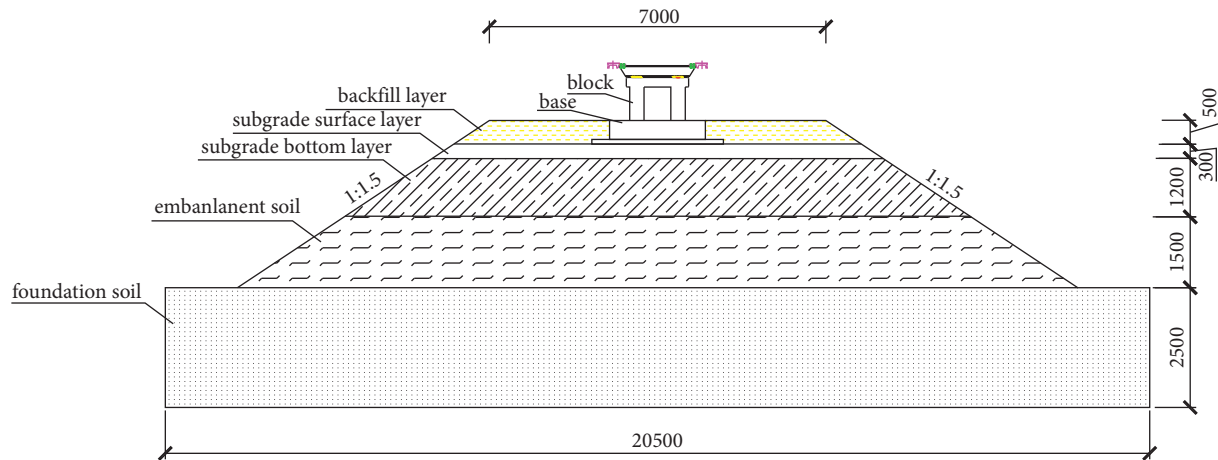


FIGURE 6: Geometric parameters of the maglev subgrade used in the FEM.

TABLE 1: Material properties considered in the FEM of the maglev subgrade.

Soil type	Density ( $\text{kg/m}^3$ )	Modulus of deformation (MPa)	Poisson's ratio	Internal friction angle ( $^\circ$ )	Cohesive force (kPa)
Backfill layer	1700	100	0.35	20	15
Base bed surface layer	Graded broken stone	2200	0.25	—	—
	Group A filler	2100	0.3	—	—
Base bed bottom layer	Gravelly soil	2000	0.3	25	20
	Coarse-grained soil	1900	0.32	20	25
	Fine-grained soil	1850	63	0.35	20
Embankment soil	1850	70	0.35	25	60
Foundation soil	1700	120	0.35	32	20

TABLE 2: Track load statistics.

Project	Material	Unit weight ( $\text{kg/m}$ )	Unit weight ( $\text{kg/m}$ )	
			1.2 m fastener spacing	0.8 m fastener spacing
F-shaped steel	Q235D	126.5 $\text{kg/m}$	253.00	253.00
Senseboard	Aluminum		6.80	6.80
Sleeper	Q235D	95.15 $\text{kg/m}$	115.33	173.00
Fastener	QT450-10, 35VB, etc.	23.16 $\text{kg/group}$	38.60	57.90
Total			413.74	490.7
Average			452.22 $\text{kg/m} \approx 4.5 \text{ kN/m}$	

## 4. Simulation Results

The material in the  $X$ -axis direction of the subgrade structure is continuous and homogeneous. When the train arrives at the middle position of the model, the dynamic load of the subgrade is the most unfavorable. The dynamic deformation and dynamic strain of the subgrade under this working condition are studied. At this time, the train load is over the model, and the top surface of the foundation bed is under the greatest stress. At this time, whether the dynamic stress, dynamic deformation, and dynamic strain of the foundation bed structure meet the requirements is determined. The cross section along the  $X$  direction of the subgrade with the largest stress distribution is selected to study the stress distribution along the depth direction.

To facilitate analysis, horizontal and vertical coordinate systems are established, as shown in Figure 6, for the horizontal and vertical directions of the subgrade structure. The surface of the subgrade is taken as a plane with a  $Z$ -axis coordinate of 0. In addition, the  $X$ -axis along the longitudinal direction of the line and the  $Y$ -axis along the transverse direction are established. The centerline of the longitudinal line is the  $X$ -axis, and the middle position along the longitudinal direction is the 0 point on the  $Y$ -axis. The coordinate system is shown in Figure 8.

**4.1. Dynamic Stress of the Subgrade Bed.** To determine the dynamic stress response of the top surface of the subgrade under the moving load, first, the working conditions of the

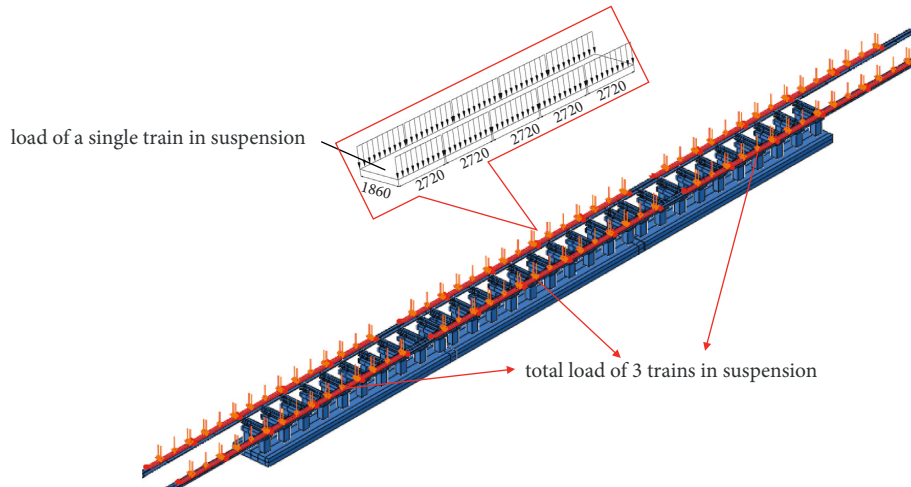


FIGURE 7: Suspended load diagram.

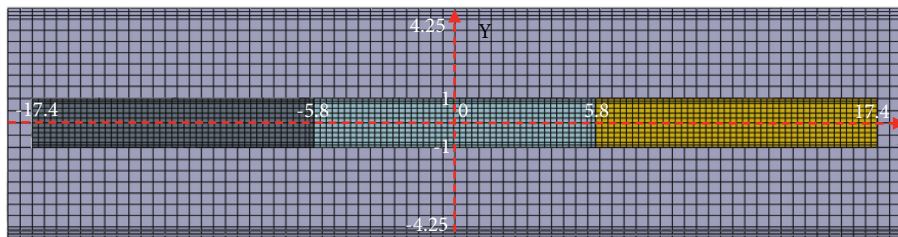


FIGURE 8: Top view coordinate map of bed structure.

train load statically placed on the model and the moving speeds of 100 km/h, 120 km/h, and 160 km/h are simulated. The maximum value of the vertical dynamic stress on the top surface of the subgrade bed is extracted under different working conditions, and the dynamic load results on the top surface of the subgrade bed are shown in Table 3.

When the design speed is 100~160 km/h, the dynamic load response of the subgrade surface increases with increasing speed, and the dynamic static stress ratio is the largest (1.182) at a speed of 160 km/h. The impact of different speeds on the surface dynamic load is generally small, with an impact difference within 10%. Therefore, the following analysis selects the most unfavorable working condition, with a speed of 160 km/h, to analyze the response of the subgrade bed.

**4.1.1. Dynamic Stress on the Top Surface of the Bed.** When the dynamic load of the train acts on the middle position of the model, the middle section is as shown in Figure 9. The white dashed frame in the figure is the outer edge of the concrete cushion, and the black dashed frame is the outer edge of the base of the rail beam. The Y coordinates of the outer edge line of the base and the cushion layer are  $\pm 1.5$  m and  $\pm 1$  m, respectively. The stress at this time is concentrated mainly on the position where the rail beam acts. In addition, the stress at the three-section base is the largest. The specific numerical analysis is as follows.

Along the longitudinal center axis of line z, the vertical stress distribution on the surface of the foundation bed is extracted. The contour diagram reveals that, along the horizontal line, the stress is not the largest at the central axis position but close to the edge of the base. Therefore, the stress distribution along the X-axis of the two places is as plotted in Figure 10(a), and the stress distribution along the Y-axis is as plotted in Figure 10(b).

The stress distribution along the X-axis direction (longitudinal) corresponds to the distribution position of the rail beam base. At the three-section base position, the stresses at the corresponding base bed positions are all large, and the maximum amplitude is essentially the same. At the expansion joint between the two bases, the stress is reduced. At  $\pm 18.4$  m, the stress is reduced to 0 due to the boundary effect of the model, and the stress distribution at the two bases adjacent to the boundary is affected to a certain extent. The position where the maximum stress on the surface of the bed is in the longitudinal direction is the middle rail beam at  $Y = \pm 0.5$  m (close to the edge of the base), and the maximum stress is approximately 13.61 kPa. At the same time, the vertical stress distribution on the central axis is relatively small, with a maximum stress value of 9.46 kPa. For the distribution of vertical stress along the Y-axis of the bed surface, the position  $X = 0$  is chosen. There are two stress peaks at  $Y = \pm 0.5$  m. These two positions are close to the edge of the base, and the stress amplitude is 13.61 kPa, while the stress at the central axis is slightly smaller, with a value of 9.46 kPa. The influence range of the stress in the transverse

TABLE 3: Dynamic load on the top surface of the bed at different speeds.

Design speed (km/h)	0 (static load)	100	120	160
Vertical stress on the surface of the base bed (kPa)	11.51	12.67	13.06	13.61
Static and static stress ratio	1	1.1	1.135	1.182

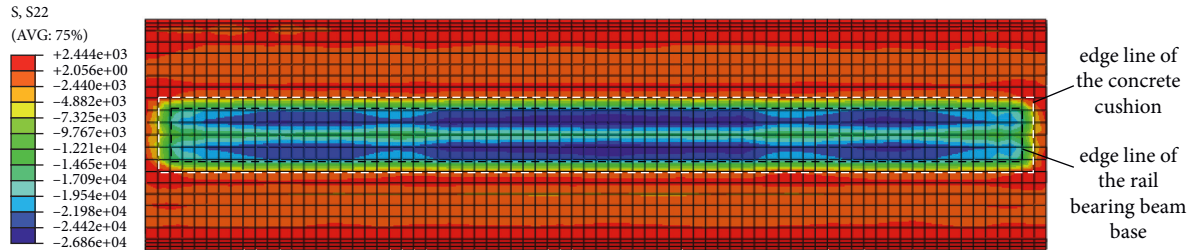


FIGURE 9: Cloud diagram of vertical stress distribution on the upper surface of the base bed.

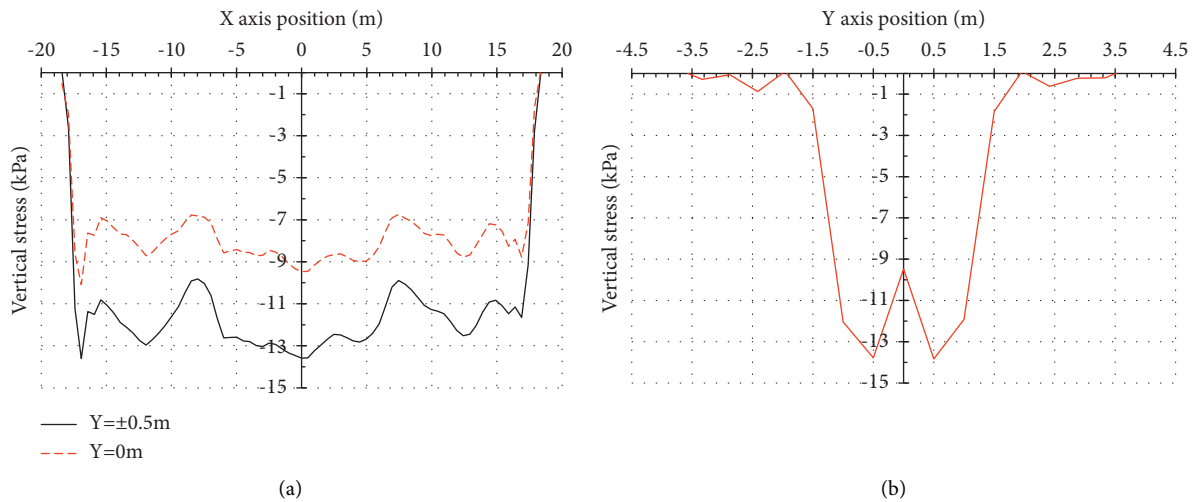


FIGURE 10: Curve of vertical stress distribution on the upper surface of the bed surface: (a) distributed along the X-axis (longitudinal); (b) distributed along the Y-axis (longitudinal).

direction is approximately 3 m, that is, the width of the concrete cushion. When the position exceeds 3 m, the stress rapidly decreases to less than 1.71 kPa, which is close to zero. The stress near the edge of the base ( $Y = \pm 0.5$  m) is approximately 43.87% larger than the stress at the central axis ( $Y = 0$ ). The conclusion can be drawn from the above analysis that, under the full load, the maximum stress on the surface of the subgrade is along  $X = 0$  (the middle position along the longitudinal direction) and  $Y = \pm 0.5$  m (the base close to the edge), and the maximum stress is approximately 13.61 kPa.

**4.1.2. Dynamic Load Influence Depth.** The maximum stress ( $X = 0$ ) is chosen to intercept the cross section and study the distribution of stress along the depth direction at this time.

Figure 11 shows the distribution cloud diagram of the vertical additional dynamic stress inside the subgrade. The maximum stress occurs at the edge of the foundation on the surface of the subgrade, and the stress decreases with increasing depth. To determine the reasonable design

thickness of the subgrade, the distribution data of the stress of the subgrade under self-weight and the stress along the depth under different subgrade fillings only under dynamic load were extracted. In addition, with reference to the design of the railway subgrade, according to the principle that the ratio of dynamic stress to subgrade self-weight stress is 0.2 produced by the train, Figure 12 can be acquired.

The attenuation curve of the additional dynamic stress along the depth shows that the attenuation is faster within the thickness of the substratum. When this stress reaches the bottom of the substratum (1.5 m), the stress attenuates significantly under different filler combinations. The combined stress attenuation effect of surface graded gravel + bottom gravel soil is the best. When the surface filler is the same, the stress attenuation effect decreases in turn when the bottom filler is gravelly soil, coarse-grained soil, and improved soil. From the figure, the reasonable design thickness of the foundation bed determined under the different foundation bed packing conditions and the attenuation of the stress in the range of the bottom of the foundation bed is as statistically shown in Table 4.

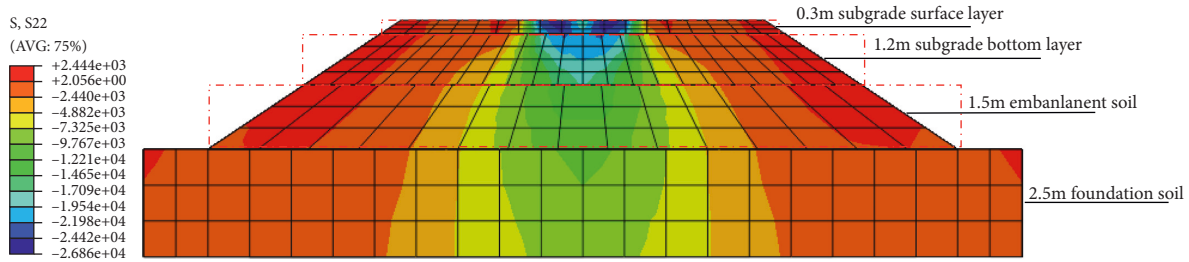


FIGURE 11: Cloud diagram of the vertical stress distribution of the subgrade bed.

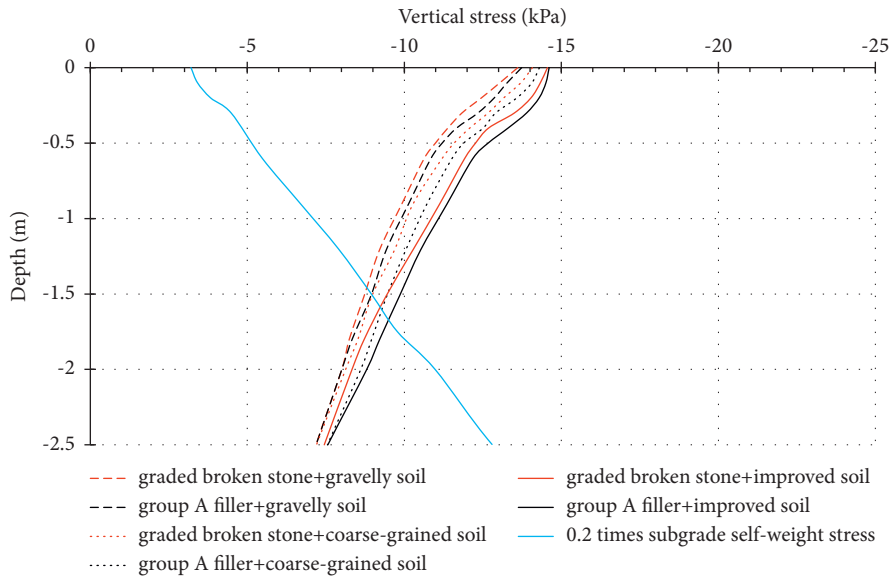


FIGURE 12: Vertical stress distribution curve of the subgrade bed.

TABLE 4: Reasonable thickness of different bed fillers.

	Working condition 1	Working condition 2	Working condition 3	Working condition 4	Working condition 5	Working condition 6
Base bed surface filler	Graded broken stone			Group a filler		
Base bed filler	Gravelly soil	Coarse-grained soil	Improved soil	Gravelly soil	Coarse-grained soil	Improved soil
Bed thickness (m)	1.46	1.50	1.59	1.49	1.60	1.70
Stress attenuation (%)	36.63	35.423	35.21	35.71	34.132	32.243

Based on the stress attenuation curve and statistics of the bed thickness table, the order of the stress attenuation effect of different bed fillers is as follows: working condition 1 > working condition 4 > working condition 2 > working condition 3 > working condition 5 > working condition 6. According to the principle that the ratio of dynamic stress to self-weight stress is 0.2, the trend in the substrate thickness is consistent with the trend in the stress attenuation effect. Therefore, the surface layer of the subgrade has the best effect with graded crushed stone + bottom gravelly soil, followed by the use of group A filler + gravelly soil on the surface.

4.2. Dynamic Deformation of the Subgrade Bed. For the deformation of the subgrade bed, the time when the middle section train acts on the middle position of the model is selected, and the deformation distribution cloud diagram of the surface of the foundation bed at this time is extracted as shown in Figure 13. The white and black dashed boxes in the figure are the concrete cushion and edge line of the rail bearing beam base, respectively. The deformation is distributed mainly in the area of the rail beam, and the base of the middle section is the main deformation position. The specific deformation distribution is as follows.

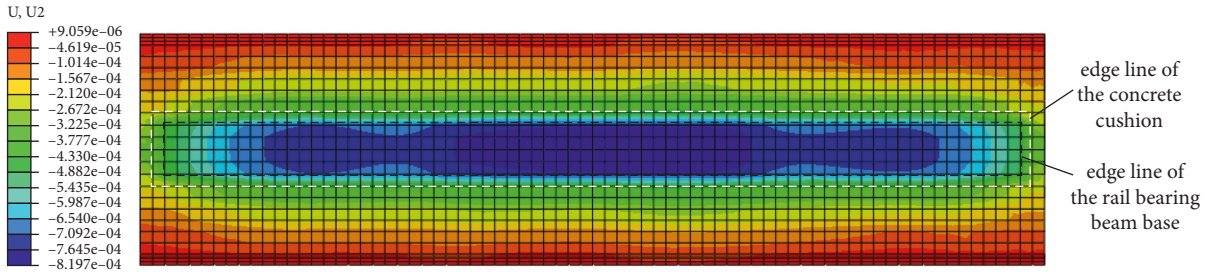


FIGURE 13: Deformation distribution cloud diagram of the surface of the foundation bed.

In the cloud diagram, the  $X$ -axis direction (longitudinal) has the largest surface deformation along the central axis, so this direction is used as a path to extract its deformation distribution value and is drawn on the graph. The  $X$ -axis middle position (coordinate 0) has the largest deformation value, so the cross section on this coordinate is chosen, and its deformation distribution curve along the  $Y$ -axis is extracted as shown here.

Combined with the cloud image, Figure 14 shows that there are three major deformation peaks along the  $X$ -axis, which correspond to the three-section rail beam base. The deformation of the middle section is consistent with the actual deformation, while the deformation of the base at both ends is affected to a certain extent due to the boundary effect of the model so that the deformation at both ends is smaller than that at the middle position. The deformation distribution along the  $Y$ -axis can be seen at the position of the coordinate at  $\pm 1$  m, and the deformation value has a more obvious turning point on the edge of the rail beam base. The distribution within  $\pm 1$  m is relatively uniform; thus, the deformation is concentrated mainly on the central axis 1 m on each side, that is, within the range of the base of the rail beam.

Statistics of the deformation of the subgrade structure under different filling conditions are shown in Table 4. Combined with the surface deformation distribution curve of the subgrade, it can be seen that the best control effect for the deformation of the subgrade is condition 1 (surface grade gravel + bottom gravel soil), followed by working condition 4 (surface layer group A filler + bottom gravel soil); the rest are working condition 2, working condition 5, working condition 3, and—finally—working condition 6.

As shown in Table 5 under working condition 1, the maximum deformation is 0.322 mm, and the deformation at the position of the expansion joint between the bases is reduced to 0.302 mm. The dynamic deformation of the working condition (condition 3, condition 6) where the bottom layer is improved soil exceeds the allowable limit of 0.4 mm. In summary, the position where the maximum deformation occurs is the  $X$ -axis origin position and the  $Y$ -axis coordinate  $\pm 0.5$  m (the edge of the base), with a maximum deformation value of 0.322 mm, which meets the maximum dynamic deformation limit of 0.4 mm in the theoretical analysis.

The location that produces the largest deformation is selected, and the cross-sectional deformation distribution cloud map is shown in Figure 15 showing that the main deformation is concentrated in the range of the bed.

**4.3. Dynamic Strain of the Subgrade Bed.** Based on the previous analysis, the position on the surface of the foundation bed with the greatest stress and deformation is determined, as well as the distribution of stress and deformation at the cross section at this location. For another control index of the foundation bed structure, the dynamic strain is determined based on the previous theoretical analysis to determine whether the maximum dynamic strain and mean dynamic strain limits are satisfied. For this purpose, the dynamic strain distribution value along the depth is extracted and plotted on a graph as shown in Figure 14.

The attenuation law of strain along the depth direction of the surface layer and the bottom layer of the subgrade is essentially the same. The strain gradually decreases with increasing depth. However, due to the difference between the surface layer and the bottom layer, a sudden change in strain occurs at the interface. The strain of the material with little difference in the modulus of deformation changes gradually, while the strain of the material with a large difference in the modulus of the surface and bottom changes significantly. This is mainly because the dynamic stress at the interface between the surface layer and the bottom layer is continuous, so the difference in value is small. From the stress-strain relationship formula (1), when the stress is continuous, the deformation modulus has a sudden change, so the corresponding strain also produces mutations.

$$\varepsilon = \frac{\sigma}{E}, \quad (1)$$

$\varepsilon$  is the strain,  $\sigma$  is the stress (MPa), and  $E$  is the deformation modulus (MPa).

The variation law of dynamic strain along the depth direction is strongly dependent on the material of the base bed under a certain load. As shown in Figure 16(a), when the surface layer is graded broken stone and group A filler, the strain values of the surface layer of the base bed are 0.0151% and 0.0173%, respectively. As the depth increases, the strain decreases. In addition, different underfills of subgrades have a certain influence on the attenuation law of surface strain. The effect can be ordered in turn as gravelly soil, grained soil, and improved soil.

The different fillers on the surface of the base bed have little effect on the strain attenuation law of the bottom layer, but when the surface layer is graded crushed stone, the strain attenuation effect is better than the working condition of the group A filler, as shown in Figure 16(b). The main influence

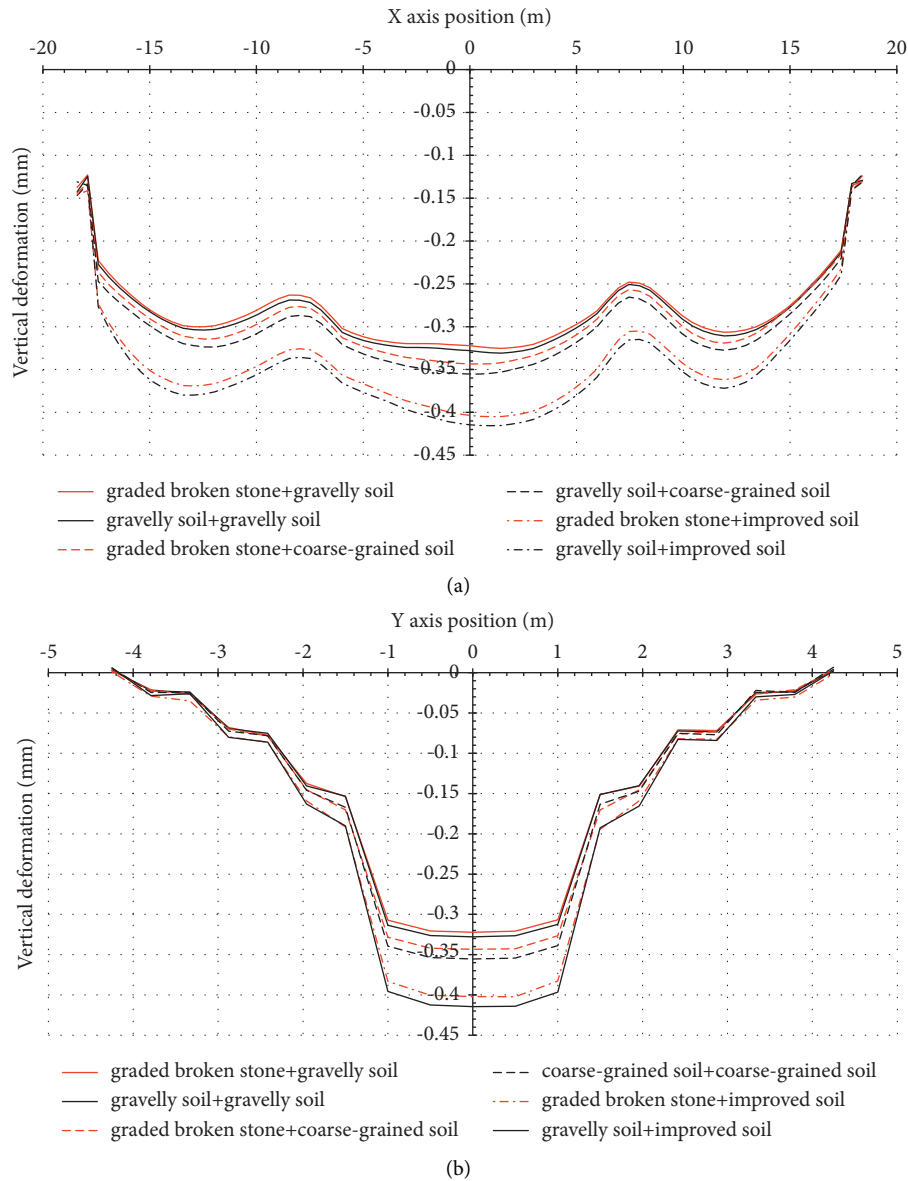


FIGURE 14: Deformation distribution curve of the surface layer of the subgrade: (a) distributed along the X-axis (longitudinal); (b) distributed along the Y-axis (horizontal).

TABLE 5: Reasonable thickness of different bed fillers.

	Working condition 1	Working condition 2	Working condition 3	Working condition 4	Working condition 5	Working condition 6
Base bed surface filler	Graded broken stone				Group A filler	
Base bed filler	Gravelly soil	Coarse-grained soil	Improved soil	Gravelly soil	Coarse-grained soil	Improved soil
Maximum deformation (mm)	0.322	0.343	0.402	0.328	0.355	0.415
Internode deformation (mm)	0.302	0.313	0.357	0.307	0.321	0.366
Dynamic deformation limit (mm)	0.4					

on the bottom layer strain attenuation law is the difference in the bottom layer filler, and the effect is significant. The maximum dynamic strain and average dynamic strain

statistics of the bottom layer under different filler conditions are shown in Table 6. The maximum dynamic strain of the bottom layer under different filler conditions all satisfies

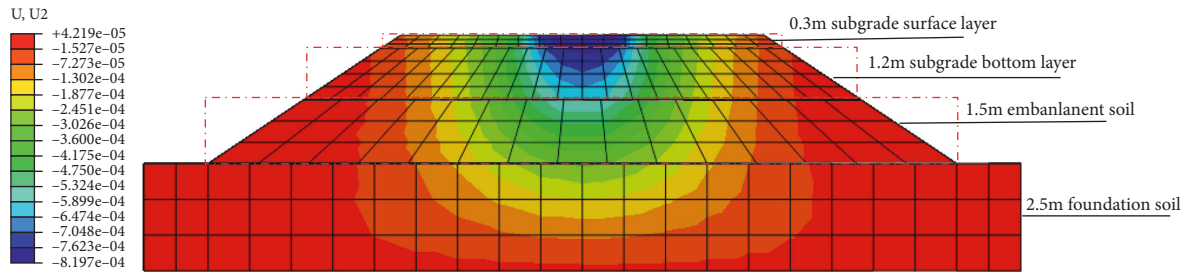


FIGURE 15: Deformation distribution cloud map of the cross section of the foundation bed.

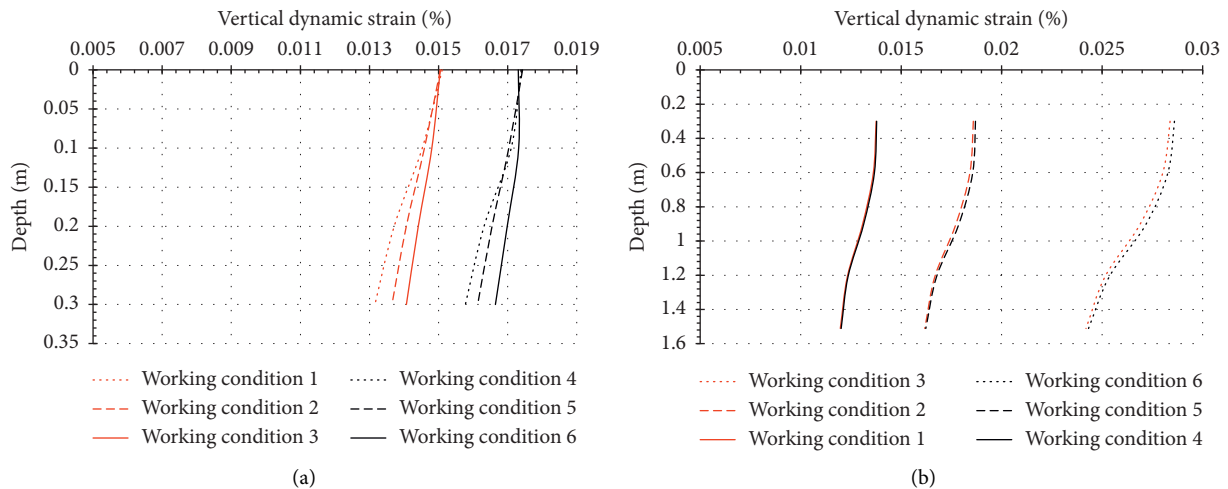


FIGURE 16: Strain distribution curve of the cross section of the foundation bed: (a) surface layer of the subgrade bed; (b) bottom of the subgrade bed.

the corresponding limits, while the only condition that the average dynamic strain index satisfies is that the bottom filler is gravel soil.

#### 4.4. Influence Analysis of the Bottom Thickness of the Subgrade.

In the analysis of the previous section, the feasibility of the 1.5 m thick foundation bed is verified by three indicators: dynamic stress, dynamic deformation, and dynamic strain. According to this analysis, this section mainly analyzes the influence of different base bed thicknesses. In addition, two sets of foundation bed thickness models are established: 1.2 m (0.3 m surface layer + 0.9 m bottom layer) and 1.8 m (0.3 m surface layer + 1.5 m bottom layer). The bottom layer of the foundation bed is analyzed to further reduce the impact on the dynamic response of the foundation bed. Figure 17 shows the dynamic stress, dynamic deformation, and average dynamic strain response diagrams under three bed thicknesses.

Based on the above analysis data:

- (1) With increasing thickness of the bottom of the foundation bed, the dynamic stress response value of the foundation bed shows a decreasing trend. However, the reduction in the stress on the upper and lower surfaces of the foundation bed is relatively small, while the stress reduction at the bottom of the

foundation bed is relatively large, indicating that the increase in the thickness of the bottom of the subgrade has a strong impact on the stress attenuation inside the bottom of the subgrade and has a certain impact on the surface of the subgrade, but the effect is small.

- (2) With increasing thickness of the bottom of the foundation bed, the dynamic deformation response law inside the foundation bed exhibits a similar trend as the stress. The deformation amount of the surface layer and the interface of the foundation bed decreases, but the decreased value is small, and the decrease law of the bottom of the foundation bed is unambiguous. However, the upper and lower surfaces of the base bed have a much smaller reduction than the bottom of the base bed.
- (3) For the dynamic strain response of the foundation bed, when the thickness of the foundation bed is 1.2 m, the average dynamic strain is 0.0133%, which exceeds the allowable average strain limit. With increasing thickness of the base bed, the average dynamic strain shows a significant decrease, but the value is relatively small.
- (4) Comprehensive analysis shows that, with increasing thickness of the bottom layer of the subgrade, the dynamic deformation and strain response of the

TABLE 6: Reasonable thickness of different bed fillers.

	Working condition 1	Working condition 2	Working condition 3	Working condition 4	Working condition 5	Working condition 6
Base bed surface filler	Graded broken stone			Group A filler		
Base bed filler	Gravelly soil	Coarse-grained soil	Improved soil	Gravelly soil	Coarse-grained soil	Improved soil
Maximum of bottom (%)	0.01376	0.0186	0.0284	0.01378	0.0187	0.0286
Threshold limit (%)	0.028	0.036	0.048	0.028	0.036	0.048
Average of bottom (%)	0.01295	0.01752	0.02652	0.01299	0.01762	0.02675
Average limit (%)	0.013	0.016	0.026	0.013	0.016	0.026

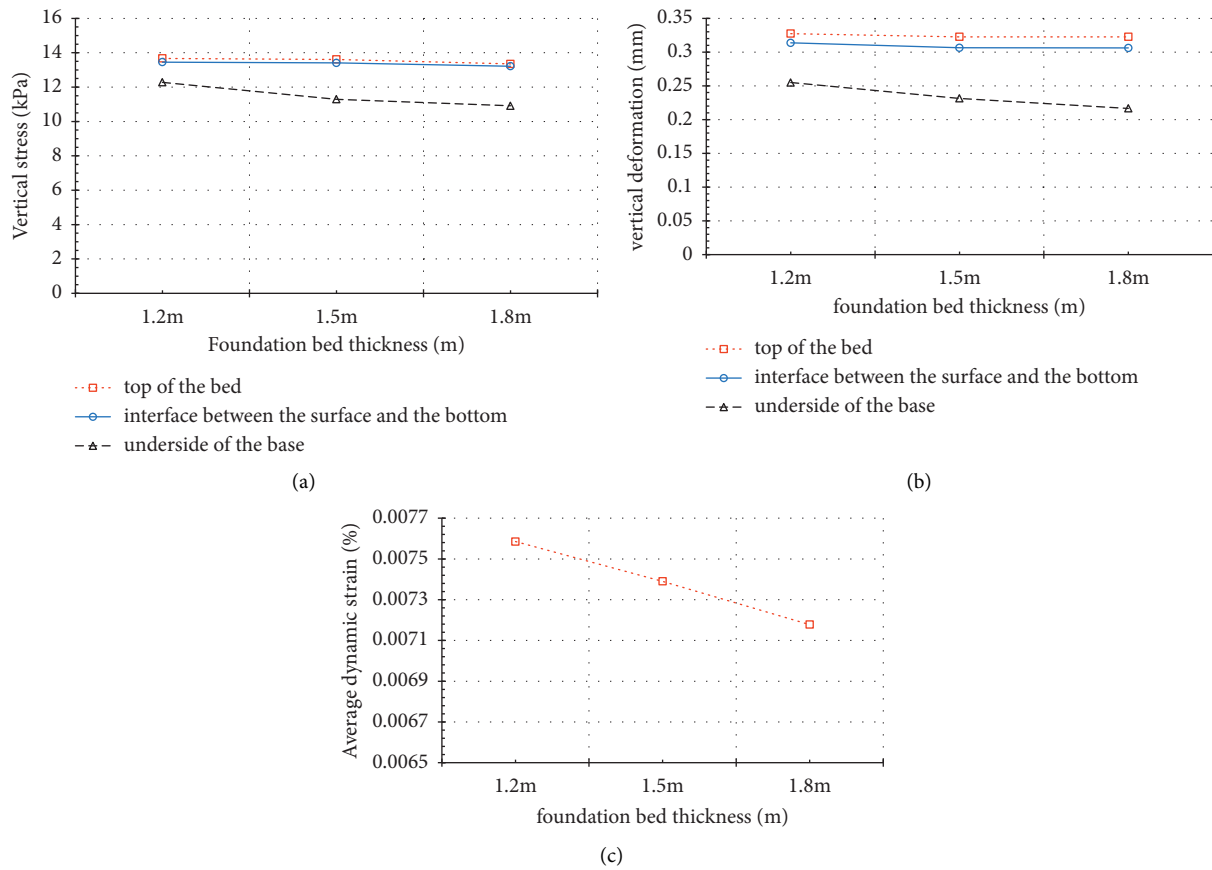


FIGURE 17: Strain distribution curve of the cross section of the foundation bed: (a) dynamic stress response; (b) deformation response; (c) dynamic strain response.

subgrade is unambiguous, while the dynamic stress response is relatively small.

- (5) The increase in the thickness of the bottom layer of the foundation bed affects mainly the dynamic stress and dynamic deformation response within the bottom layer of the foundation bed and has relatively little effect on the surface layer of the foundation bed.

The above charts and analysis establish that, under the working condition of a 1.5 m thick bed, further changes in the bed thickness affect the dynamic response of the bed.

Increasing the thickness of the bed improves the strain and stress attenuation effect of the bed; thus, the driving is safer, so no further analysis is performed here. However, reducing the thickness of the bottom layer worsens the dynamic response of the foundation bed. Here, further statistical analysis can be conducted on the indicators under the working condition of the 1.2 m foundation bed thickness. The specific conditions are shown in Table 7.

When the thickness of the bed is 1.2 m, the surface dynamic stress, dynamic deformation, maximum dynamic strain, and average dynamic strain indexes are 13.67 kPa,

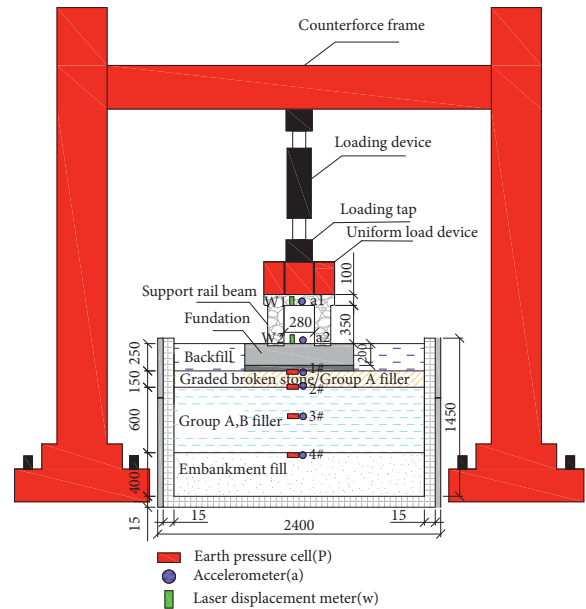
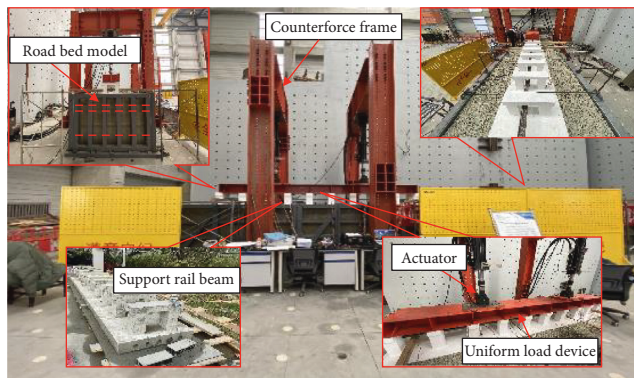
TABLE 7: Dynamic response results of the 1.2 m thick foundation bed.

1.2 m thick foundation bed	Maximum dynamic stress (kPa)	Maximum dynamic deformation (mm)	Maximum dynamic strain (%)	Average dynamic strain (%)
Response value	13.67	0.327	0.0146	0.0133
Limit value	—	0.4	0.028	0.013

TABLE 8: Comparison of technical standards for an MLS Maglev structure.

Indexes for comparison	High-speed railway design codes [39]	Zhuzhou test line	Changsha maglev express line	This study
Surface layer of subgrade bed	Thickness/m	0.4 (0.7)	—	0.3
	Filler type	Graded crushed rock	Graded crushed rock	Graded crushed rock rock/group A filler
Bottom layer of subgrade bed	Thickness/m	2.3	—	1.2
	Filler type	Group A, B filler/improved soil	Graded crushed rock	Group A, B filler Gravelly soil

Note. The thickness of the surface layer is 0.4 m on the track of the high-speed railway without ballasts and 0.7 m on the track of a high-speed railway with ballasts.



(a)

(b)

FIGURE 18: Continued.

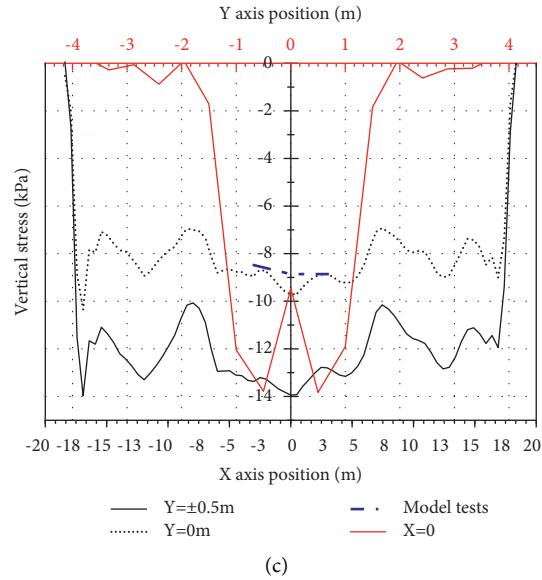


FIGURE 18: Comparison of model test and results: (a) Physical picture of model. (b) Schematic diagram of cross section of model test. (c) Comparison curve of vertical stress distribution on the upper surface of bed surface.

0.327 mm, 0.0146%, and 0.0133%, respectively. At this time, the average dynamic strain index is outside the specification limit. Thus, adopting this scheme has certain risks. When the thickness is increased to 1.5 m and 1.8 m, the dynamic deformation and dynamic strain of the foundation bed are improved.

## 5. Discussion of Results

Based on the research results of this study, the recommended indexes for the selection criteria of the subgrade bed structure thickness and subgrade filler type for the MLS maglev structure are given. The research results of this study are compared with current high-speed railway design codes and the application achievements of the Zhuzhou test line and Changsha Maglev Express Line in Table 8.

This study has reasonably optimized the relevant technical indicators of the MLS maglev subgrade bed structure and made corresponding reductions based on existing construction experience and previously reported application results. Therefore, the results of this study are more economical and reasonable.

In addition, researchers from NEDL of Southwest Jiaotong University are currently conducting research on the MLS magnetic levitation low-mounted structure roadbed bed in conjunction with the current status of research on the low-middle-speed magnetic levitation low-mounted structure roadbed bed, relying on the 2018 Science and Technology Major Project (2018-A01) "Engineering Application Research on the Complete Set of Technology of Low-Middle Speed Magnetic Levitation Transportation System" of China Railway Construction Co. model tests related to this study, as shown in Figures 18(a) and 18(b).

Since the model test related to this research is still underway, and the collection and analysis of related test data are also underway, this study only focuses on the comparison and

analysis of the numerical simulation and model test on the dynamic stress of the subgrade bed. The numerical simulation coordinates corresponding to the surface stress of the subgrade bed at the position of the longitudinal center axis of the extracted model test and the position under the loading plate are shown in Figure 18(c). At the position of  $X=0$  m, the numerical simulation result is 9.46 kPa, and the model test result is 8.86 kPa; at the position of  $X=\pm 3$  m, the numerical simulation results are 8.99 kPa and 8.66 kPa, and the model test results are 8.85 kPa and 8.48 kPa, which consists with the general law, indicating that the numerical model is reliable.

## 6. Conclusion

In this study, the numerical model of MLS maglev structure laid on the ground is established using ABAQUS, and the analysis and research are carried out, taking into account the current status of research on the roadbed of low and medium-speed maglev low placement structure. The following conclusions are obtained:

- (1) By simulating the actual load, it is found that the magnitude of stress acting on the surface of the subgrade at different speeds has an insignificant influence, and the difference is within 10%. Therefore, the most unfavorable load condition (speed of 160 km/h) is used for the calculations to obtain the dynamic stress of the subgrade surface with a value of 13.61 kPa. The maximum stress occurs at the middle of the longitudinal rail bearing beam. The depth of influence of dynamic load is about 1.5 m calculated by the principle that the ratio of dynamic stress to the self-weight stress of the roadbed is 0.2. When the surface filler is group A filler, the influence depth of the bottom filler is coarse-grained soil and improved soil increases to 1.6 m and 1.7 m, respectively. When

the surface filler is graded gravel and the bottom layer is gravel soil, the influence depth of dynamic load is the smallest (1.46 m), and the stress attenuation to the bottom of the bed is about 36.63%.

- (2) The distribution of dynamic deformation on the surface of the subgrade bed is uniform in the horizontal direction within the range of the base (2 m). The maximum deformation is concentrated mainly in the range of 0.5 m on both sides of the central axis, the maximum value of the dynamic deformation distribution along the longitudinal direction occurs in the middle of the rail beam position, and the deformation at the internode position is reduced. The minimum dynamic deformation is 0.322 mm for a surface filler of graded gravel and a bottom layer of gravel soil. The dynamic strain is analyzed by the two indexes of maximum dynamic strain and average dynamic strain. The maximum dynamic strain meets the limit under all working conditions, and the average dynamic strain meets the requirements except for the two working conditions where the bottom layer is gravel soil.
- (3) By summarizing the working conditions determined by the above indicators, when the thickness of the base bed is 1.5 m, the surface layer is graded crushed stone or group A filler, and the bottom layer uses crushed stone soil. In this case, the bed can meet the dynamic stress, dynamic deformation, and dynamic strain indicators. The change in the thickness of the subgrade has a certain influence on the dynamic response of the subgrade. Among the relevant factors, the influence on the dynamic strain is the largest. When the thickness of 1.5 m meets the requirements, the average dynamic strain obtained by further reducing the thickness of the subgrade exceeds the limit.

Through the above conclusions, it is recommended that the thickness of the base bed is set at 1.5 m, the surface layer of filler is graded gravel or group A filler, and the bottom layer uses gravel soil.

## Data Availability

The data involved are contained in the article.

## Conflicts of Interest

The authors declare that they have no conflicts of interest.

## Acknowledgments

This research was funded by China Railway Construction Co. Ltd, Grant no. 2018-A01, and funded by National Natural Science Foundation of China, Grant no. 51978588.

## References

- [1] L. Luguang Yan, "Development and application of the maglev transportation system," *IEEE Transactions on Applied Superconductivity*, vol. 18, no. 2, pp. 92–99, 2008.
- [2] J. S. Wang, S. Y. Wang, Y. W. Zeng et al., "The present status of the high temperature superconducting Maglev vehicle in China," *Superconductor Science and Technology*, vol. 18, no. 2, pp. S215–S218, 2005.
- [3] M. Zhai, Z. Long, and X. Li, "Calculation and evaluation of load performance of magnetic levitation system in medium-low speed maglev train," *International Journal of Applied Electromagnetics and Mechanics*, vol. 61, no. 4, pp. 519–536, 2019.
- [4] Y. Sun, H. Qiang, J. Xu, and G. Lin, "Internet of Things-Based Online Condition Monitor and Improved Adaptive Fuzzy Control for a Medium-Low-Speed Maglev Train System," *IEEE Transactions on Industrial Informatics*, vol. 16, no. 4, 2020.
- [5] X. Lu, Y. Li, M. Wu, J. Zuo, and W. Hu, "Rail temperature rise characteristics caused by linear eddy current brake of high-speed train," *Journal of Traffic and Transportation Engineering*, vol. 1, no. 6, pp. 448–456, 2014.
- [6] J. Hu, W. Ma, X. Chen, and S. Luo, "Levitation Stability and Hopf Bifurcation of EMS Maglev Trains," *Mathematical Problems in Engineering*, vol. 2020, Article ID 2936838, 12 pages, 2020.
- [7] H. Yu, J. Jiao, E. Houston, and Z. R. Peng, "Evaluating the relationship between rail transit and industrial agglomeration: an observation from the Dallas-fort worth region, TX," *Journal of Transport Geography*, vol. 67, 2018.
- [8] B. Zeng, "The adaptability and the improvement in engineering of the lower - medium speed maglev transit system," *Journal of Railway Engineering Society*, vol. 33, no. 10, pp. 111–115, 2016.
- [9] J. Sadeghi, H. Liravi, and M. H. Esmaeili, "Experimental investigation on loading pattern of railway concrete slabs," *Construction and Building Materials*, vol. 153, pp. 481–495, 2017.
- [10] J. A. Sadeghi and M. H. Esmaeili, "Effectiveness of Track Stiffness Reduction in Attenuation of Metro Induced Vibrations Received by Historical Buildings," *Latin American Journal of Solids and Structures*, vol. 15, no. 11, 2018.
- [11] P. Leng, J. Li, and Y. Jin, "Kinematics modeling and analysis of mid-low speed maglev vehicle with screw and product of exponential theory," *Symmetry*, vol. 11, no. 10, p. 1201, 2019.
- [12] J. Geng, *Theory and Experimental Research of Key Parameters Design on Simply-Supported Track Girders of Low to Medium Speed Malev line*, Southwest Jiaotong University, Sichuan, China, 2018.
- [13] C. Wen-Feng, X. U. Xi-Jiang, W. U. Cheng-Jin, and Y. Ping, *Research on Key Technologies in Track Design of Zhuzhou Medium and Low Speed Maglev Transit Test Line*, Railway Standard Design, Uttar Pradesh, India, 2015, In Chinese.
- [14] De Ping-Yang, J. Liu, Li. Xiao-Zhen, and Y. Ping, "Investigation of dynamic factors of low and medium speed maglev simply-supported guideway beam," *Bridge Construction*, vol. 46, no. 4, pp. 79–84, 2016, In Chinese.
- [15] P. Yang, Yu-L. Zhan, Li. Xiao-Zhen, and Y. Ping, "Study of track beam stiffness of medium and low speed maglev test line," *World Bridges*, vol. 44, no. 3, pp. 58–62, 2016, In Chinese.
- [16] B. S. Gao and F. Z. Xiao, "Dynamic characteristics analysis of low set line structure of medium and low speed maglev transit," *HIGH SPEED RAILWAY TECHNOLOGY*, vol. 6, no. 4, pp. 36–39+76, 2015, In Chinese.
- [17] Li. Xiao-Zhen, J. Geng, D. X. Wang, X. Zhang, and L. Lin, "Study on vertical coupling vibration of low-medium speed maglev train and at-ground-structure system," *Engineering Mechanics*, vol. 34, no. 12, pp. 210–218+247, 2017, In Chinese.

- [18] D.-X. Wang, *Study on Space Coupling Vibration of Low-Medium Speed Maglev Train and At-Ground structure*, Southwest Jiaotong University, Sichuan, China, 2015.
- [19] Z. Ding, "Optimization of key technical standards for ground structure of Changsha maglev express," *Railway Standard Design*, vol. 63, no. 6, pp. 6–10, 2019.
- [20] P. Han, "Comparison and analysis of main technical standards of Germany and China high speed railway subgrade," *Journal of Railway Engineering*, vol. 34, no. 4, pp. 21–24, 2017.
- [21] D. Liang, K. Zhang, Q. Jiang, and Y. Wang, "A novel analytic method to calculate the equivalent stray capacitance of the low-speed maglev train's suspension electromagnet," *Energies*, vol. 13, no. 20, p. 5469, 2020.
- [22] N. Hu, G.-L. Dai, B. Yan, and K. Liu, "Recent development of design and construction of medium and long span high-speed railway bridges in China," *Engineering Structures*, vol. 74, pp. 233–241, 2014.
- [23] S. Maximov, F. Gonzalez-Montañez, R. Escarela-Perez, J. C. Olivares-Galvan, and H. Ascencion-Mestiza, "Analytical analysis of magnetic levitation systems with harmonic voltage input," *Actuators*, vol. 9, no. 3, p. 82, 2020.
- [24] S. Bhowmick and G.-R. Liu, "Three dimensional CS-FEM phase-field modeling technique for brittle fracture in elastic solids," *Applied Sciences*, vol. 8, no. 12, p. 2488, 2018.
- [25] O. Hibi, "Automatically operated maglev public transport line in Nagoya," *ELEKTRISCHE BAHNEN-CHARLOTTENBURG THEN BERLIN THEN MUNCHEN*, vol. 104, no. 10, p. 480, 2006.
- [26] D. Y. Doh Young Park, B. C. Byung Chun Shin, and H. Hyungsuk Han, "Korea's urban maglev program," *Proceedings of the IEEE*, vol. 97, no. 11, pp. 1886–1891, 2009.
- [27] J. Guardo, "Magnetic levitation transport system," *U.S. Patent Application*, vol. 301, pp. 26–4, 2007.
- [28] K. Xie, *Medium and Low Speed Maglev Based on UM and ANSYS Co-simulationcoupled Vibration Analysis of Vehicle-Track Beam system*, Southwest Jiaotong University, Sichuan, China, 2019.
- [29] Y. Ming, *Research on Changsha Medium and Low Speed Maglev Gauges*, Railway Standard Design, Lucknow, Uttar, vol. 63, no. 2, p. 7, 2017.
- [30] Q. L. Jiang, J. S. Lian, and D. K. Yue, "Mechanical Coupling Analysis of Single EMS Module," *Journal of The China Railway Society*, 2005.
- [31] S. Li-Wei, "Research on the Lightweight of the Beam of Maglev Train," *Journal of Jiamusi University(Natural ence Edition)*, 2018.
- [32] Z. Lin, "Tangshan mid and low-speed maglev test line contact rail reformed—the replacement of steel-aluminum contact rail engineering practice," *Modern Urban Transit*, vol. 8, no. 1, pp. 83–92, 2012.
- [33] M. Li, *Research on Coupling Vibration of Mid-low Speed Maglev Vehicle on Light Switch Steel beam*, Southwest Jiaotong University, Sichuan, China, 2018.
- [34] *Code for Design of Railway Earth Structure TB10001-2016*.
- [35] H. Xie, *Engineering Application of Medium and Low Speed Maglev Traffic system*, pp. 60–77, China railway publishing house CO. LTD, China, 2018.
- [36] J. Sadeghi and M. H. Esmaeili, "Safe distance of cultural and historical buildings from subway lines," *Soil Dynamics and Earthquake Engineering*, vol. 96, pp. 89–103, 2017.
- [37] M. H. Esmaeili, M. Naeimi, B. Soltani, and M. Afsartaha, "Reducing slab track vibrations by using asphalt concrete in the substructure," in *Proceedings of the Joint Rail Conference American Society of Mechanical Engineers (ASME)*, Columbia, SC, USA, April 2016.
- [38] *Basic Technical Parameters of Changsha Maglev vehicle(CS\_XT-JK-000 A)2014-04-30*.
- [39] TB 10621-2014, *Code for Design of High Speed Railway*.